

Event patterns (particle scatter plots) extracted from charged particle spectra in pp and Pb-Pb collisions at 2.76 TeV

Ya-Hui Chen^a, Fu-Hu Liu^{a,1}, Sakina Fakhreddin^{b,c}, Magda A. Rahim^{b,c}, Mai-Ying Duan^a

^a*Institute of Theoretical Physics, Shanxi University, Taiyuan, Shanxi 030006, China*

^b*Department of Physics, College of Science and Arts at Riyadh Al Khabrah, Qassim University, Buraidah 51452, Al Qassim, Saudi Arabia*

^c*Department of Physics, Faculty of Science, Sana'a University, P.O. Box 1247, Sana'a, Yemen*

Abstract: The transverse momentum (p_T) and pseudorapidity (η) spectra of charged particles produced in proton-proton (pp) and lead-lead (Pb-Pb) collisions at the large hadron collider (LHC) are described by a hybrid model. In the model, the p_T spectrum is described by a two-component distribution which contains an inverse power-law suggested by the QCD (Quantum Chromodynamic) calculus and an Erlang distribution resulted from a multisource thermal model. The η spectrum is described by a Gaussian rapidity (y) distribution resulted from the Landau hydrodynamic model and the two-component p_T distribution, where the conversion between y and η is accurately considered. The modelling results are in agreement with the experimental data measured by the ATLAS Collaboration in pp collisions at center-of-mass energy $\sqrt{s} = 2.76$ TeV and in Pb-Pb collisions at center-of-mass energy per nucleon pair $\sqrt{s_{NN}} = 2.76$ TeV. Based on the parameter values extracted from p_T and η or y spectra, the event patterns or particle scatter plots in three-dimensional velocity and momentum spaces are obtained.

Keywords: Transverse momentum spectrum, (pseudo)rapidity spectrum, event pattern, particle scatter plot

PACS: 12.38.Mh, 25.75.Dw, 24.10.Pa

1 Introduction

The relativistic heavy ion collider (RHIC) and the large hadron collider (LHC) have been opening a new epoch for high-energy nucleus-nucleus (heavy ion) collisions, in which not only the quark-gluon plasma (QGP) is created, but also more abundant phenomena on multi-particle productions are discovered [1–7]. High-energy nucleus-nucleus collisions at the RHIC and LHC can form a condition of high temperature and density. The evolution and decay of the interacting system at high temperature and density is a complex process, in which only limited information can be measured in experiments due to technical and economical reasons. To understand the whole interacting system as minutely as possible, the method of event reconstruction and reappearance is used in the modelling analyses. By using the method of event reconstruction and reappearance, we can obtain partly the

¹E-mail: fuhuliu@163.com; fuhuliu@sxu.edu.cn

event patterns or particle scatter plots at the stage of kinetic freeze-out of the interacting system. Generally, the event patterns (particle scatter plots) are expected to be different in descriptions for different particles produced in different collisions at different energies.

To reconstruct and reappear the event patterns (particle scatter plots) at kinetic freeze-out, we need at least the transverse momentum (p_T) and rapidity (y) or pseudorapidity (η) spectra. The p_T spectrum reflects the transverse excitation degree, and the y or η spectrum reflects the longitudinal expansion degree, of the interacting system. To describe the p_T spectrum, one has used more than ten functions which include, but are not limited to, the standard distribution [8, 9], Tsallis statistics [10–12], Schwinger mechanism [13–16], Erlang distribution [17], inverse power-law [18–20], and so forth. Among these functions, some of them (standard distribution, Tsallis statistics, and Erlang distribution) are based on thermal or statistical reason, and others (Schwinger mechanism and inverse power-law) are based on the QCD (Quantum Chromodynamic) calculus. Generally, the spectrum in low- p_T region is described by the thermal and statistical distributions, and the spectrum in high- p_T region is described by the QCD calculus. Exceptionally, the Schwinger mechanism describes only the spectrum in low- p_T region, and the Tsallis statistics describes a wide spectrum. In most case, one needs a two-component distribution to describe the p_T spectrum.

To describe the y spectrum, one has the Gaussian distribution [21–24], two-Gaussian distribution [25], three-Gaussian distributions [26], and other modelling descriptions such as the three-fireball model [27–32], the three-source relativistic diffusion model [33–36], and the model with two Tsallis (or Boltzmann-Gibbs) clusters of fireballs [37–39]. The Gaussian y distribution is resulted from the Landau hydrodynamic model and its revisions [21–24], the two-Gaussian y distribution [25] can be resulted from a two-component Landau hydrodynamic model in which the two Gaussian distributions correspond to the contributions in the backward and forward y regions, respectively, and the three-Gaussian y distribution is resulted from the three-component Landau hydrodynamic model in which the third Gaussian distributions correspond to the contribution in the central y region [26]. It should be noticed that the backward and forward y regions are relative in collider experiments. Even if for the backward, forward, and central y regions, there are alternative methods to describe the y spectrum such as the three-fireball [27–32] or three-source model [33–36] which results in other y distributions. Most models describe the y spectrum to be arithmetic solutions than analytic one.

In our recent works [40, 41], the event patterns (particle scatter plots) extracted from the spectra of net-baryons produced in central gold-gold (Au-Au) collisions at RHIC energies, and from the spectra of Z bosons and quarkonium states (some charmonium $c\bar{c}$ mesons and bottomonium $b\bar{b}$ mesons) produced in proton-proton (pp) and lead-lead (Pb-Pb) collisions at LHC energies, were reported. As a successor, the present work presents the event patterns (particle scatter plots) extracted from the spectra of charged particles produced in pp collisions at the center-of-mass energy $\sqrt{s} = 2.76$ TeV and in Pb-Pb collisions at the center-of-mass energy per nucleon pair $\sqrt{s_{NN}} = 2.76$ TeV [42] which are one of LHC energies. Comparing with our recent works [40, 41], we use different functions for p_T and y spectra in the present work, which reflects the flexibility of the model and method used by us.

The rest part of this paper is structured as followings. The model and method are concisely described in section 2. Results and discussion are given in section 3. In section

4, we summarize our main observations and conclusions.

2 The model and method

The model used in the present work is a hybrid model, in which the p_T spectrum is described by a two-component distribution which contains an inverse power-law suggested by the QCD calculus [18–20] and an Erlang distribution resulted from a multisource thermal model [17], and the y spectrum is described by a Gaussian distribution resulted from the Landau hydrodynamic model [21–24]. The η spectrum is also described due to the Gaussian y distribution and the two-component p_T distribution, where the conversion between y and η is accurately considered.

According to the QCD calculus [18–20], the p_T spectrum in high- p_T region is described by the inverse power-law

$$f_1(p_T) = Ap_T \left(1 + \frac{p_T}{p_0}\right)^{-n}, \quad (1)$$

where p_0 and n are free parameters, and A is the normalization constant which results in $\int_0^\infty f_1(p_T) dp_T = 1$ and is related to the free parameters. According to the multisource thermal model [17], the Erlang distribution which describes the p_T spectrum for a given sample is given by

$$f_2(p_T) = \frac{p_T^{m-1}}{(m-1)! \langle p_{Ti} \rangle^m} \exp\left(-\frac{p_T}{\langle p_{Ti} \rangle}\right), \quad (2)$$

where $\langle p_{Ti} \rangle$ and m are free parameters. We can use $f_1(p_T)$ and $f_2(p_T)$ to describe the hard scattering process and soft excitation process respectively. Let k denote the contribution ratio (relative contribution) of the hard process, the final p_T spectrum is described by the two-component distribution

$$f_{p_T}(p_T) = kf_1(p_T) + (1-k)f_2(p_T). \quad (3)$$

According to the Landau hydrodynamic model [21–24], the interacting system can be described by the hydrodynamics, which results in the y spectrum to be a Gaussian function [23, 24]

$$f_y(y) = \frac{1}{\sqrt{2\pi}\sigma_y} \exp\left[-\frac{(y-y_C)^2}{2\sigma_y^2}\right], \quad (4)$$

where σ_y denotes the dispersion or width of rapidity distribution and y_C denotes the peak position or mid-rapidity. In symmetric collisions such as in pp and Pb-Pb collisions at the LHC discussed in the present work, we have $y_C = 0$ in the laboratory or center-of-mass reference frame. The experimental η spectrum is also described by the Gaussian y distribution and the two-component p_T distribution, in the case of the conversion between y and η is accurately considered by a Monte Carlo method. In some cases, the y spectrum is described by two Gaussian distributions, one is for the backward y region and the other one is for the forward y region. In the case of considering the three Gaussian distributions, the third one is for the central y region.

In the Monte Carlo method, let $R_{1,2,3,4}$ and r_i ($i = 1, 2, \dots, m$) denote random numbers distributed evenly in $[0,1]$. We have

$$\int_0^{p_T} f_1(p_T) dp_T < R_1 < \int_0^{p_T+dp_T} f_1(p_T) dp_T \quad (5)$$

due to Eq. (1), where p_T in the upper limit of integral changes from 0 to the maximum. Or

$$p_T = -\langle p_{Ti} \rangle \sum_{i=1}^m \ln r_i = -\langle p_{Ti} \rangle \ln \prod_{i=1}^m r_i \quad (6)$$

due to Eq. (2).

$$y = \sigma_y \sqrt{-2 \ln R_2} \cos(2\pi R_3) + y_C \quad (7)$$

due to Eq. (4). The azimuth φ can be given by

$$\varphi = 2\pi R_4 \quad (8)$$

due to φ distributing evenly in $[0, 2\pi]$ for an isotropic source in the transverse plane.

In the considered reference frame such as the laboratory or center-of-mass reference frame, the energy E is given by

$$E = \sqrt{p_T^2 + m_0^2} \cosh y, \quad (9)$$

where m_0 denotes the rest mass of the considered particle. In the case of considering unidentified charged particles, we take $m_0 = 0.174 \text{ GeV}/c^2$ which is estimated from an average weighted the masses and yields of different types of charged particles [7]. The x -, y -, and z -components of momentum and velocity are given by

$$p_x = p_T \cos \varphi, \quad p_y = p_T \sin \varphi, \quad p_z = \sqrt{p_T^2 + m_0^2} \sinh y, \quad (10)$$

and

$$\beta_x = \frac{p_x}{E}, \quad \beta_y = \frac{p_y}{E}, \quad \beta_z = \frac{p_z}{E} = \tanh y, \quad (11)$$

respectively. The polar angle θ and the pseudorapidity η can be given by

$$\theta = \arctan \left(\frac{p_T}{p_z} \right) \quad (12)$$

and

$$\eta \equiv -\ln \tan \left(\frac{\theta}{2} \right) \quad (13)$$

respectively.

In the above discussions, a series of values of η can be obtained due to the Gaussian y distribution (Eq. (4)) and the two-component p_T distribution (Eq. (3)), where the conversion between y and η is accurately considered by the Monte Carlo calculation. Then, the final η distribution is obtained by the statistics. At the same time, based on the Monte Carlo calculation, a series of values of velocity and momentum components can be obtained. Then, we can present and compare the event patterns (particle scatter plots) in the three-dimensional velocity and momentum spaces at the stage of kinetic freeze-out of the interacting system for different particles produced in different collisions at different energies, where different particles may produce at different stages of collisions and carry

different information of interactions.

3 Results and discussion

Figure 1 presents the transverse momentum spectra, $d^2\sigma/(p_T d\eta dp_T)$, of charged particles produced in pp collisions at $\sqrt{s} = 2.76$ TeV and in Pb-Pb collisions at $\sqrt{s_{NN}} = 2.76$ TeV in the pseudorapidity interval $|\eta| < 2$, where σ denotes the cross-section, and the integral luminosity $L_{\text{int}}^{\text{pp}} = 4.2 \text{ pb}^{-1}$ for pp collisions and $L_{\text{int}}^{\text{PbPb}} = 0.15 \text{ nb}^{-1}$ for Pb-Pb collisions. The symbols represent the experimental data of the ATLAS Collaboration [42], where the data for Pb-Pb collisions are divided by $\langle T_{AA} \rangle$ which is estimated as the number of nucleon-nucleon collisions over their cross section [42, 43], and multiplied by different amounts marked in the panel. The curves are our results calculated by using the two-component p_T distribution (Eq. (3)). In the calculation, the method of least squares is used to determine the values of parameters when we do the fit to experimental data. The values of free parameters (p_0 , n , k , m , and $\langle p_{Ti} \rangle$), normalization constants (N_{p_T}), and χ^2 per degree of freedom (χ^2/dof) are listed in Table 1, where the normalization constant N_{p_T} is used to give comparison between the normalized curve with experimental data, and the values of m in the Erlang distribution are invariably taken to be 2 which are not listed in the column. One can see that the results calculated by using the hybrid model are in agreement with the experimental p_T data of charged particles produced in pp and Pb-Pb collisions at 2.76 TeV measured by the ATLAS Collaboration. The values of p_0 , n , and k for the inverse power-law increase with the decrease of centrality (or with the increase of centrality percentage), and the values of $\langle p_{Ti} \rangle$ for the Erlang distribution does not show an obvious tendency with the decrease of centrality. The contributions of inverse power-law are not always main. We shall discuss further the characteristics of parameters in the latter part of this section.

Figures 2 and 3 are the same as those for Figure 1, but they show the results in different $|\eta|$ intervals in pp and 0–5% Pb-Pb collisions, respectively. The values of free parameters (p_0 , n , k , m , and $\langle p_{Ti} \rangle$), normalization constants (N_{p_T}), and χ^2 per degree of freedom (χ^2/dof) are listed in Table 1, where the values of m in the Erlang distribution are invariably taken to be 2 which are not listed in the column. One can see that the results calculated by using the hybrid model are in agreement with the experimental p_T data of charged particles with different $|\eta|$ intervals in pp and 0–5% Pb-Pb collisions at 2.76 TeV measured by the ATLAS Collaboration. The values of p_0 increases slightly and $\langle p_{Ti} \rangle$ decreases slightly with the increase of $|\eta|$ in pp collisions, and they do not show an obvious tendency in 0–5% Pb-Pb collisions. With the increase of $|\eta|$, n increases and k does not change in both pp and 0–5% Pb-Pb collisions. Once again, the contributions of inverse power-law are not always main.

Based on the two-component p_T distribution in which the parameter values are obtained from Figure 1, and the Gaussian y distribution in which the parameter values need to be determined, we can perform the Monte Carlo calculation and obtain a series of values of η . Thus, the η distribution is obtained by the statistics. Figure 4 shows the η spectra of charged particles produced in pp and Pb-Pb collisions at 2.76 TeV for four p_T intervals: (a) $1.7 < p_T < 2.0 \text{ GeV}/c$, (b) $6.7 < p_T < 7.7 \text{ GeV}/c$, (c) $19.9 < p_T < 22.8 \text{ GeV}/c$, and (d) $59.8 < p_T < 94.8 \text{ GeV}/c$. The symbols represent the experimental data

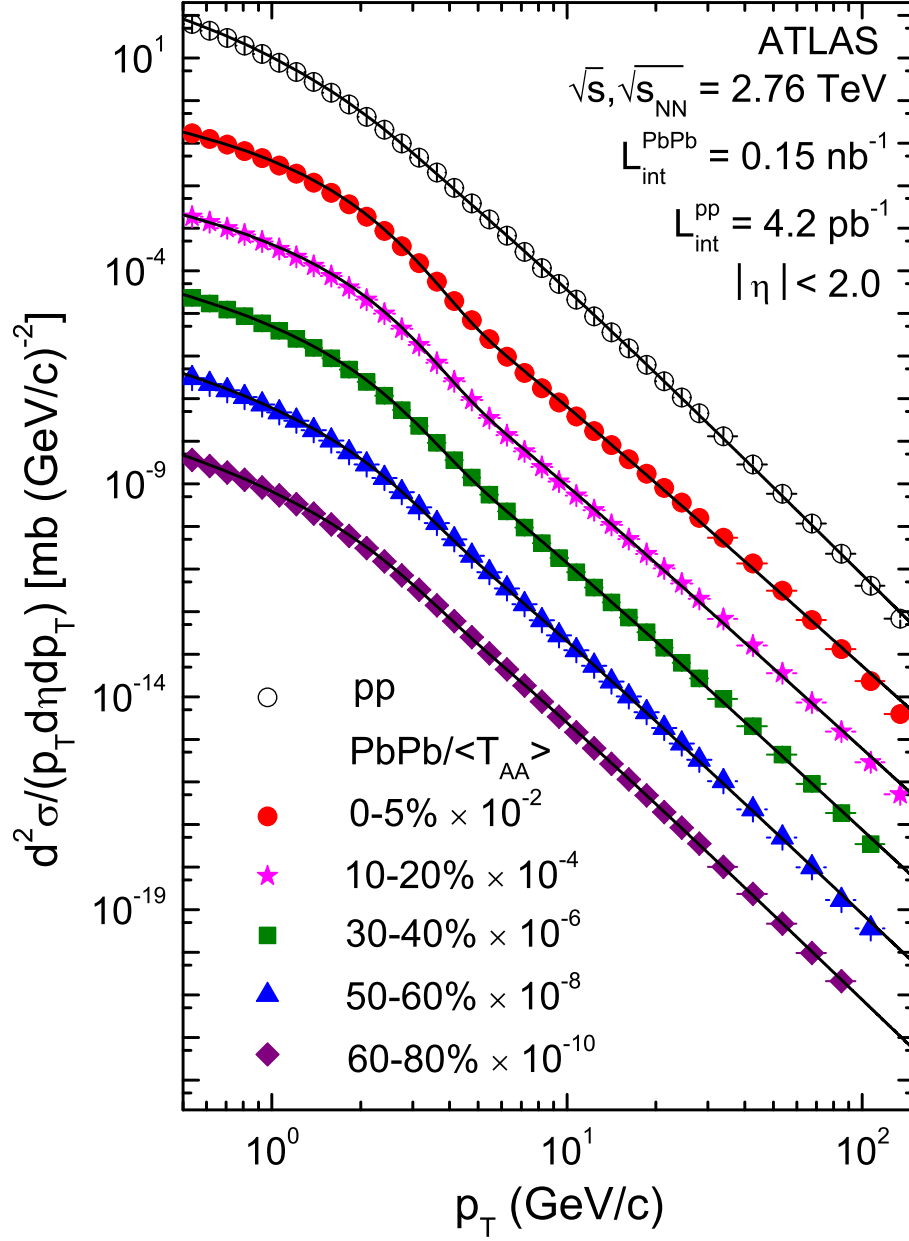


Fig. 1. Transverse momentum spectra of charged particles produced in pp and Pb-Pb collisions at 2.76 TeV. The symbols represent the data measured by the ATLAS Collaboration [42] and the curves are our results calculated by using the two-component distribution. For different centrality intervals, the spectra are multiplied by different amounts marked in the panels.

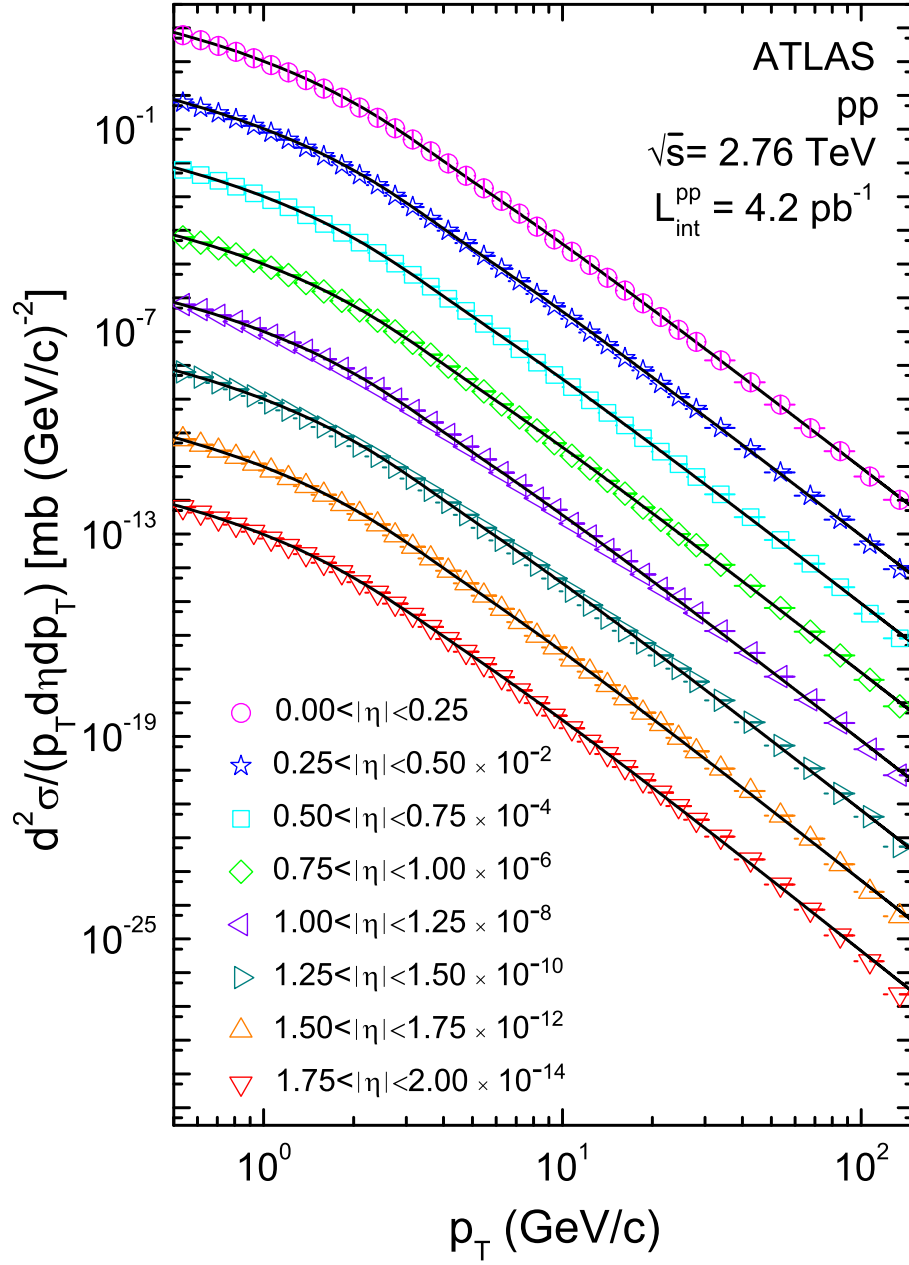


Fig. 2. Same as Figure 1, but showing the results in different pseudorapidity ranges in pp collisions.

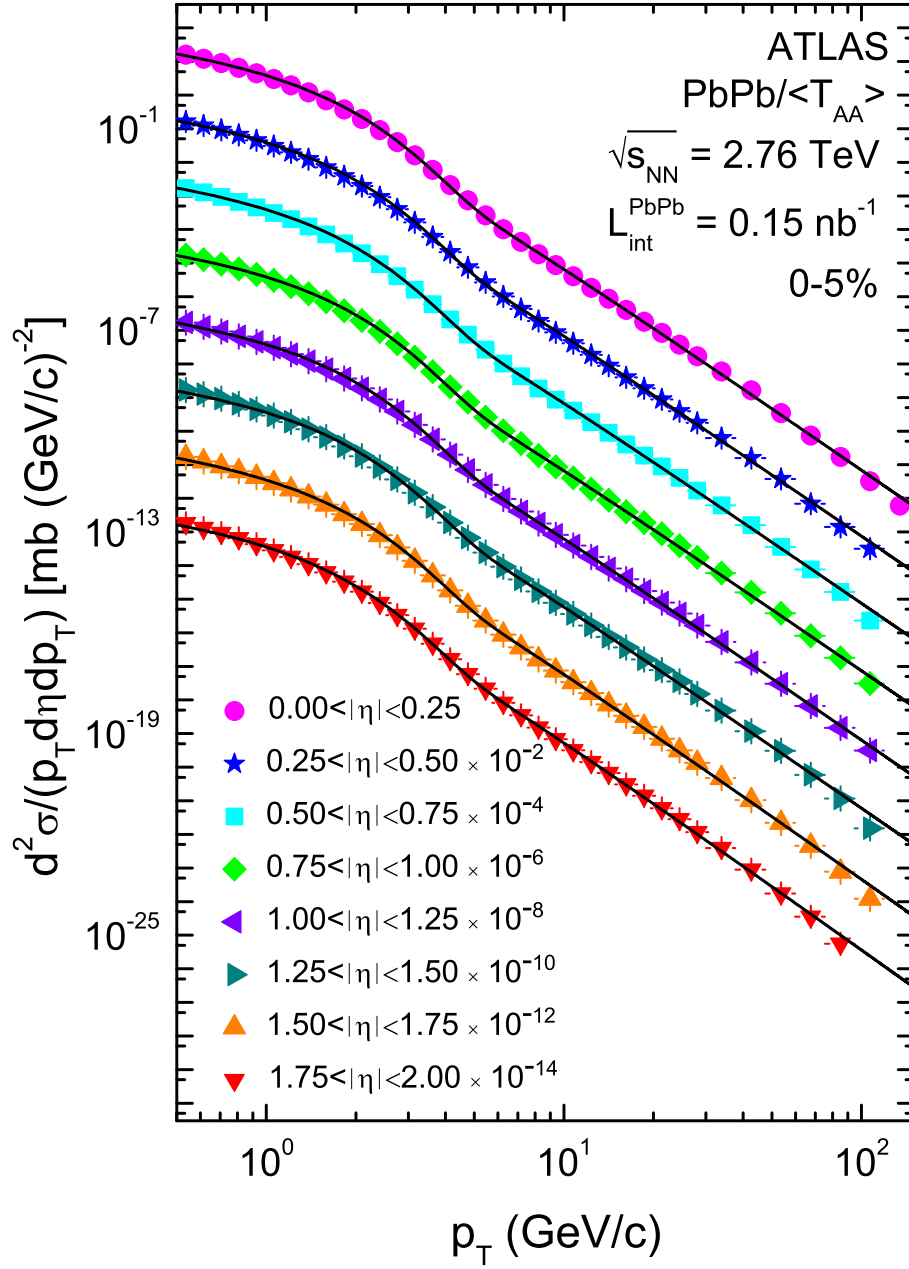


Fig. 3. Same as Figure 1, but showing the results in different pseudorapidity ranges in 0–5% Pb-Pb collisions.

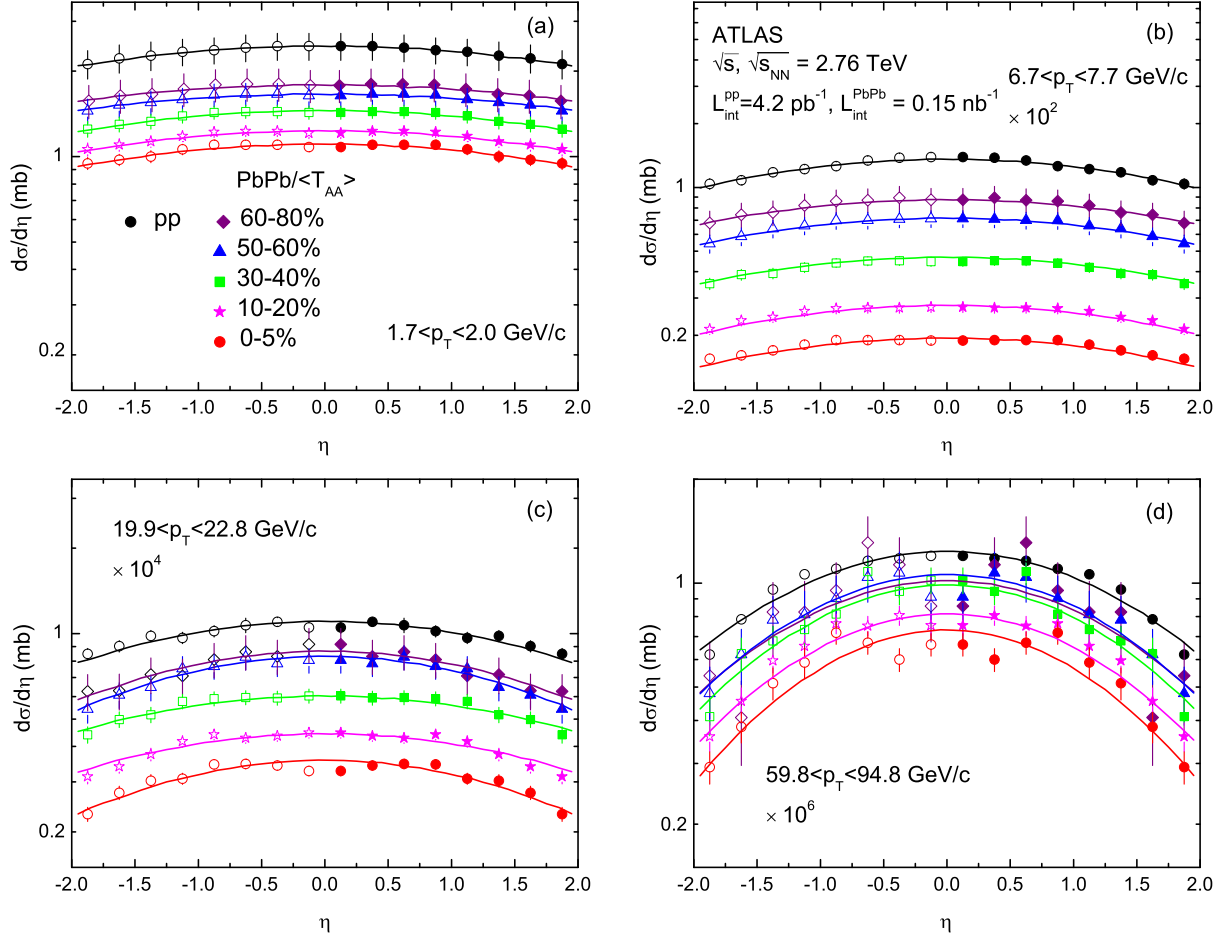


Fig. 4. Pseudorapidity spectra of charged particles produced in pp and Pb-Pb collisions at 2.76 TeV for four p_T intervals: (a) $1.7 < p_T < 2.0$ GeV/ c , (b) $6.7 < p_T < 7.7$ GeV/ c , (c) $19.9 < p_T < 22.8$ GeV/ c , and (d) $59.8 < p_T < 94.8$ GeV/ c . The symbols represent the data measured by the ATLAS Collaboration [42] and the curves are our results calculated by using the Gaussian y distribution (and the two-component p_T distribution), where the conversion between y and η is considered. For different transverse momentum intervals, the spectra are multiplied by different amounts marked in the panels.

measured by the ATLAS Collaboration [42] and the curves are our results calculated by the Gaussian y distribution and the two-component p_T distribution, where the conversion between y and η is considered. For different p_T intervals, the spectra are multiplied by different amounts marked in the panels. The values of free parameters (σ_y and y_C), normalization constants (N_y), and χ^2/dof are listed in Table 2, where the normalization constant N_y is used to give comparison between the normalized curve with experimental data, and the values of y_C are not listed in the column due to $y_C = 0$ at all time. One can see that the results calculated by using the hybrid model are approximately in agreement with the experimental η data of charged particles produced in pp and Pb-Pb collisions at 2.76 TeV measured by the ATLAS Collaboration. The width of rapidity distribution decreases with the increases of p_T and centrality. Although the Gaussian y distribution in some cases has a space to be extended to the two-Gaussian y distribution [41], only the Gaussian y distribution is approximately used in the present work due to a representation of the methodology.

Further, based on the parameter values obtained from Figures 1 and 4, we can perform the Monte Carlo calculation and obtain a series of values of kinematical quantities. As a diagrammatic sketch, Figure 5 presents the event patterns (particle scatter plots) in the three-dimensional velocity ($\beta_x - \beta_y - \beta_z$) space at the kinetic freeze-out of the interacting system formed in pp collisions for four p_T intervals: (a) $1.7 < p_T < 2.0$ GeV/ c , (b) $6.7 < p_T < 7.7$ GeV/ c , (c) $19.9 < p_T < 22.8$ GeV/ c , and (d) $59.8 < p_T < 94.8$ GeV/ c . The blue and red globules represent the contributions of inverse power-law and Erlang distribution respectively, where the red globules in the second p_T intervals are highlighted for clarity. The number of particles for each panel is 1000. The values of root-mean-squares ($\sqrt{\beta_x^2}$ for β_x , $\sqrt{\beta_y^2}$ for β_y , and $\sqrt{\beta_z^2}$ for β_z) and the maximum $|\beta_x|$, $|\beta_y|$, and $|\beta_z|$ ($|\beta_x|_{\max}$, $|\beta_y|_{\max}$, and $|\beta_z|_{\max}$) are listed in Table 3 which are obtained by higher statistics. The relative yields of particle numbers appearing in different p_T intervals are listed in Table 4, where the relative yield in the highest p_T interval is taken to be 1. One can see that the contributions of inverse power-law are main in the first two p_T intervals, and sole in the last two p_T intervals. The contribution of Erlang distribution can be neglected in the second p_T interval. The relations $\sqrt{\beta_x^2} \approx \sqrt{\beta_y^2} \ll \sqrt{\beta_z^2}$ and $|\beta_x|_{\max} \approx |\beta_y|_{\max} \approx |\beta_z|_{\max} \approx 1$ render that the root-mean-square velocities form an ellipsoid surface with the major axis along the beam direction, and the maximum velocities form a spherical surface.

By using the same method as that for Figure 5, we can obtain the similar results in Pb-Pb collisions with centrality intervals 60–80%, 50–60%, 30–40%, 10–20%, and 0–5%, respectively. The values of root-mean squares of velocity components and the maximum velocity components are listed in Table 3, and the relative yields of particle numbers appearing in different p_T intervals are listed in Table 4. As an example, to reduce the size of the paper file, only the scatter plots in the three-dimensional velocity space in 0–5% Pb-Pb collisions are given in Figure 6. Some conclusions obtained from Figures 1 and 5 can be obtained from Figure 6 and Tables 3 and 4. In addition, we see intuitively the density change of particle numbers in the three-dimensional velocity space in different p_T intervals at the kinetic freeze-out of the interacting system formed in Pb-Pb collisions with different centrality intervals.

Table 1. Values of free parameters (p_0 , n , k , m , and $\langle p_{Ti} \rangle$), normalization constant (N_{p_T}), and χ^2/dof corresponding to the curves in Figures 1–3, where the values of m in the Erlang distribution are invariably taken to be 2 which are not listed in the column.

Figure	Type	p_0 (GeV/c)	n	k	$\langle p_{Ti} \rangle$ (GeV/c)	N_{p_T}	χ^2/dof
Figure 1	pp	0.82 ± 0.04	6.90 ± 0.10	0.90 ± 0.05	0.37 ± 0.02	345.0 ± 17.3	6.634
	PbPb, $C = 0\text{--}5\%$	0.66 ± 0.03	6.24 ± 0.10	0.41 ± 0.05	0.38 ± 0.02	72.3 ± 3.6	12.476
	PbPb, $C = 10\text{--}20\%$	0.70 ± 0.04	6.34 ± 0.10	0.50 ± 0.05	0.39 ± 0.02	83.8 ± 4.2	10.719
	PbPb, $C = 30\text{--}40\%$	0.72 ± 0.04	6.44 ± 0.10	0.63 ± 0.05	0.39 ± 0.02	115.5 ± 5.8	4.926
	PbPb, $C = 50\text{--}60\%$	0.75 ± 0.04	6.59 ± 0.10	0.76 ± 0.05	0.39 ± 0.02	164.1 ± 8.2	1.686
	PbPb, $C = 60\text{--}80\%$	0.78 ± 0.04	6.70 ± 0.10	0.85 ± 0.05	0.40 ± 0.02	202.2 ± 10.1	0.681
Figure 2	pp , $0.00 < \eta < 0.25$	0.85 ± 0.04	6.85 ± 0.10	0.87 ± 0.05	0.39 ± 0.02	304.0 ± 15.2	5.458
	pp , $0.25 < \eta < 0.50$	0.85 ± 0.04	6.86 ± 0.10	0.87 ± 0.05	0.39 ± 0.02	306.8 ± 15.3	5.575
	pp , $0.50 < \eta < 0.75$	0.85 ± 0.04	6.87 ± 0.10	0.88 ± 0.05	0.39 ± 0.02	304.3 ± 15.2	6.399
	pp , $0.75 < \eta < 1.00$	0.86 ± 0.04	6.90 ± 0.10	0.88 ± 0.05	0.39 ± 0.02	299.6 ± 15.0	6.355
	pp , $1.00 < \eta < 1.25$	0.86 ± 0.04	6.91 ± 0.10	0.87 ± 0.05	0.38 ± 0.02	301.1 ± 15.1	6.218
	pp , $1.25 < \eta < 1.50$	0.87 ± 0.04	6.95 ± 0.10	0.87 ± 0.05	0.38 ± 0.02	295.9 ± 14.8	5.127
	pp , $1.50 < \eta < 1.75$	0.88 ± 0.05	7.01 ± 0.10	0.87 ± 0.05	0.37 ± 0.02	295.2 ± 14.8	5.675
	pp , $1.75 < \eta < 2.00$	0.90 ± 0.05	7.08 ± 0.10	0.88 ± 0.05	0.35 ± 0.02	297.1 ± 14.9	6.574
Figure 3	PbPb, $0.00 < \eta < 0.25$	0.67 ± 0.04	6.13 ± 0.10	0.36 ± 0.05	0.39 ± 0.02	67.3 ± 3.4	12.044
	PbPb, $0.25 < \eta < 0.50$	0.65 ± 0.04	6.10 ± 0.10	0.35 ± 0.05	0.39 ± 0.02	67.5 ± 3.4	12.713
	PbPb, $0.50 < \eta < 0.75$	0.65 ± 0.03	6.10 ± 0.10	0.35 ± 0.05	0.39 ± 0.02	67.6 ± 3.4	12.566
	PbPb, $0.75 < \eta < 1.00$	0.65 ± 0.03	6.10 ± 0.10	0.35 ± 0.05	0.39 ± 0.02	67.4 ± 3.4	10.751
	PbPb, $1.00 < \eta < 1.25$	0.66 ± 0.03	6.14 ± 0.10	0.35 ± 0.05	0.39 ± 0.02	66.2 ± 3.3	7.959
	PbPb, $1.25 < \eta < 1.50$	0.66 ± 0.03	6.14 ± 0.10	0.35 ± 0.05	0.39 ± 0.02	62.3 ± 3.1	8.215
	PbPb, $1.50 < \eta < 1.75$	0.68 ± 0.03	6.26 ± 0.10	0.39 ± 0.05	0.39 ± 0.02	62.7 ± 3.1	9.323
	PbPb, $1.75 < \eta < 2.00$	0.70 ± 0.03	6.33 ± 0.10	0.38 ± 0.05	0.38 ± 0.02	64.1 ± 3.2	7.913

Table 2. Values of free parameter (σ_y and y_C), normalization constant (N_η), and χ^2/dof corresponding to the curves in Figure 4, where the values of y_C are not listed in the column due to $y_C = 0$ at all time.

Figure	Type	σ_y	N_η	χ^2/dof
Figure 4(a) $1.7 < p_T < 2.0$ GeV/c	pp	3.40 ± 0.17	92.80 ± 4.64	0.003
	PbPb, 60–80%	3.80 ± 0.19	68.40 ± 3.42	0.037
	PbPb, 50–60%	3.80 ± 0.19	63.50 ± 3.18	0.046
	PbPb, 30–40%	3.30 ± 0.17	54.80 ± 2.74	0.137
	PbPb, 10–20%	3.30 ± 0.17	46.50 ± 2.33	0.518
	PbPb, 0–5%	3.20 ± 0.16	41.60 ± 2.08	0.661
Figure 4(b) $6.7 < p_T < 7.7$ GeV/c	pp	2.50 ± 0.13	0.49 ± 0.02	0.687
	PbPb, 60–80%	2.70 ± 0.14	0.32 ± 0.02	0.086
	PbPb, 50–60%	2.60 ± 0.13	0.26 ± 0.01	0.142
	PbPb, 30–40%	2.60 ± 0.13	0.17 ± 0.01	1.324
	PbPb, 10–20%	2.50 ± 0.13	0.10 ± 0.01	1.116
	PbPb, 0–5%	2.50 ± 0.13	0.07 ± 0.01	1.856
Figure 4(c) $19.9 < p_T < 22.8$ GeV/c	pp	2.40 ± 0.12	$(3.95 \pm 0.20) \times 10^{-3}$	1.643
	PbPb, 60–80%	2.20 ± 0.11	$(3.04 \pm 0.15) \times 10^{-3}$	0.461
	PbPb, 50–60%	2.10 ± 0.11	$(2.88 \pm 0.14) \times 10^{-3}$	0.469
	PbPb, 30–40%	2.30 ± 0.12	$(2.19 \pm 1.11) \times 10^{-3}$	1.002
	PbPb, 10–20%	2.10 ± 0.11	$(1.59 \pm 0.08) \times 10^{-3}$	3.064
	PbPb, 0–5%	2.01 ± 0.10	$(1.24 \pm 0.06) \times 10^{-3}$	4.665
Figure 4(d) $59.8 < p_T < 94.8$ GeV/c	pp	1.70 ± 0.09	$(4.00 \pm 0.20) \times 10^{-5}$	3.310
	PbPb, 60–80%	1.60 ± 0.08	$(3.21 \pm 0.16) \times 10^{-5}$	3.865
	PbPb, 50–60%	1.55 ± 0.08	$(3.30 \pm 0.17) \times 10^{-5}$	0.813
	PbPb, 30–40%	1.52 ± 0.08	$(3.05 \pm 0.15) \times 10^{-5}$	2.829
	PbPb, 10–20%	1.50 ± 0.08	$(2.50 \pm 0.13) \times 10^{-5}$	2.718
	PbPb, 0–5%	1.40 ± 0.07	$(2.17 \pm 0.11) \times 10^{-5}$	6.708

Figure 7 presents the event patterns (particle scatter plots) in the three-dimensional momentum ($p_x - p_y - p_z$) space at the kinetic freeze-out of the interacting system formed in pp collisions for four p_T intervals: (a)(b) $1.7 < p_T < 2.0$ GeV/c, (c)(d) $6.7 < p_T < 7.7$

GeV/c, (e)(f) $19.9 < p_T < 22.8$ GeV/c, and (g)(h) $59.8 < p_T < 94.8$ GeV/c. The left and right panels display the results in a wide (from -1.5 to 1.5 TeV/c) and narrow (from -50 to 50 GeV/c) p_z ranges respectively. The blue and red globules represent the contributions of inverse power-law and Erlang distribution respectively, where the red globules in the second p_T interval are highlighted for clarity. The number of particles for each panel in the left is 1000. The values of root-mean-squares ($\sqrt{p_x^2}$ for p_x , $\sqrt{p_y^2}$ for p_y , and $\sqrt{p_z^2}$ for p_z) and the maximum $|p_x|$, $|p_y|$, and $|p_z|$ ($|p_x|_{\max}$, $|p_y|_{\max}$, and $|p_z|_{\max}$) are listed in Table 5. The relative yields of particle numbers appearing in different p_T intervals are listed in Table 4, and the percentages of particle numbers in the interval $-50 < p_z < 50$ GeV/c over whole p_z range for different p_T intervals are listed in Table 6, where “PL” in Table 6 denotes the “power-law”. One can see that some conclusions obtained from Figures 5 and 6 can be obtained from Figure 7. In the wide p_z range, most particles constitute a circle-like region surrounded by a few particles. In the narrow p_z range, particles constitute a cylinder surface surrounded by a few particles. We have the relations $\sqrt{p_x^2} \approx \sqrt{p_y^2} \ll \sqrt{p_z^2}$ and $|p_x|_{\max} \approx |p_y|_{\max} \ll |p_z|_{\max}$.

Table 3. Values of the root-mean-squares $\sqrt{\beta_x^2}$ for β_x , $\sqrt{\beta_y^2}$ for β_y , and $\sqrt{\beta_z^2}$ for β_z , as well as the maximum $|\beta_x|$, $|\beta_y|$, and $|\beta_z|$ ($|\beta_x|_{\max}$, $|\beta_y|_{\max}$, and $|\beta_z|_{\max}$) corresponding to the scatter plots in different types of collisions, where the corresponding scatter plots in pp and 0–5% Pb-Pb collisions are presented in Figures 5 and 6 respectively. Both the root-mean-squares and the maximum velocity components are in the units of c , and all the p_T intervals are in the units of GeV/c.

Type	$\sqrt{\beta_x^2}$	$\sqrt{\beta_y^2}$	$\sqrt{\beta_z^2}$	$ \beta_x _{\max}$	$ \beta_y _{\max}$	$ \beta_z _{\max}$
<i>pp</i>						
$1.7 < p_T < 2.0$	0.328 ± 0.010	0.343 ± 0.010	0.879 ± 0.006	0.993	0.994	1.000
$6.7 < p_T < 7.7$	0.359 ± 0.010	0.343 ± 0.010	0.868 ± 0.006	0.995	0.997	1.000
$19.9 < p_T < 22.8$	0.361 ± 0.010	0.354 ± 0.010	0.863 ± 0.006	1.000	0.996	1.000
$59.8 < p_T < 94.8$	0.413 ± 0.009	0.391 ± 0.009	0.823 ± 0.007	0.999	0.999	0.999
<i>PbPb, 60–80%</i>						
$1.7 < p_T < 2.0$	0.331 ± 0.010	0.336 ± 0.010	0.880 ± 0.006	0.992	0.994	1.000
$6.7 < p_T < 7.7$	0.358 ± 0.010	0.347 ± 0.010	0.867 ± 0.006	0.995	0.997	1.000
$19.9 < p_T < 22.8$	0.368 ± 0.010	0.332 ± 0.009	0.869 ± 0.006	1.000	0.995	1.000
$59.8 < p_T < 94.8$	0.405 ± 0.009	0.390 ± 0.009	0.827 ± 0.006	0.998	0.995	0.999
<i>PbPb, 50–60%</i>						
$1.7 < p_T < 2.0$	0.324 ± 0.010	0.331 ± 0.010	0.885 ± 0.006	0.992	0.994	1.000
$6.7 < p_T < 7.7$	0.354 ± 0.010	0.351 ± 0.010	0.866 ± 0.006	0.995	0.997	1.000
$19.9 < p_T < 22.8$	0.364 ± 0.010	0.334 ± 0.009	0.869 ± 0.006	1.000	0.988	1.000
$59.8 < p_T < 94.8$	0.399 ± 0.009	0.386 ± 0.009	0.832 ± 0.006	0.998	1.000	0.999
<i>PbPb, 30–40%</i>						
$1.7 < p_T < 2.0$	0.325 ± 0.009	0.350 ± 0.010	0.877 ± 0.006	0.993	0.994	1.000
$6.7 < p_T < 7.7$	0.362 ± 0.010	0.344 ± 0.010	0.866 ± 0.006	0.995	0.997	1.000
$19.9 < p_T < 22.8$	0.374 ± 0.010	0.358 ± 0.010	0.856 ± 0.006	1.000	0.996	1.000
$59.8 < p_T < 94.8$	0.414 ± 0.009	0.389 ± 0.009	0.823 ± 0.006	0.995	0.999	0.999
<i>PbPb, 10–20%</i>						
$1.7 < p_T < 2.0$	0.325 ± 0.009	0.350 ± 0.010	0.877 ± 0.006	0.993	0.994	1.000
$6.7 < p_T < 7.7$	0.362 ± 0.010	0.344 ± 0.010	0.866 ± 0.006	0.995	0.997	1.000
$19.9 < p_T < 22.8$	0.374 ± 0.010	0.358 ± 0.010	0.856 ± 0.006	1.000	0.996	1.000
$59.8 < p_T < 94.8$	0.413 ± 0.009	0.389 ± 0.009	0.823 ± 0.006	0.995	0.999	0.999
<i>PbPb, 0–5%</i>						
$1.7 < p_T < 2.0$	0.343 ± 0.010	0.353 ± 0.010	0.869 ± 0.006	0.993	0.992	1.000
$6.7 < p_T < 7.7$	0.369 ± 0.010	0.348 ± 0.010	0.862 ± 0.006	0.995	0.997	1.000
$19.9 < p_T < 22.8$	0.378 ± 0.010	0.356 ± 0.009	0.855 ± 0.006	1.000	0.995	1.000
$59.8 < p_T < 94.8$	0.419 ± 0.009	0.388 ± 0.009	0.821 ± 0.007	0.995	0.999	0.999

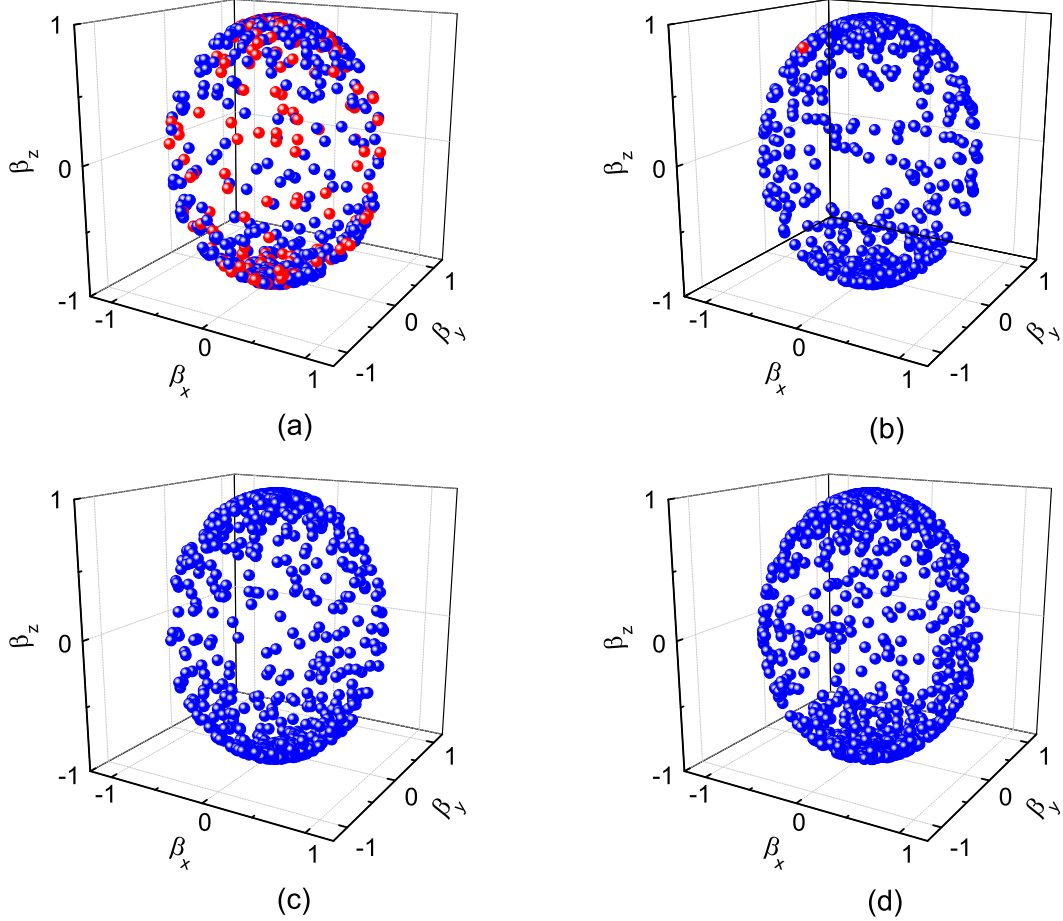


Fig. 5. Event patterns (particle scatter plots) in three-dimensional velocity ($\beta_x - \beta_y - \beta_z$) space at kinetic freeze-out in pp collisions for four transverse momentum intervals: (a) $1.7 < p_T < 2.0$ GeV/ c , (b) $6.7 < p_T < 7.7$ GeV/ c , (c) $19.9 < p_T < 22.8$ GeV/ c , and (d) $59.8 < p_T < 94.8$ GeV/ c . The velocity components are in the units of c . The blue and red globules represent the contributions of inverse power-law and Erlang distribution respectively. The number of particles for each panel is 1000.

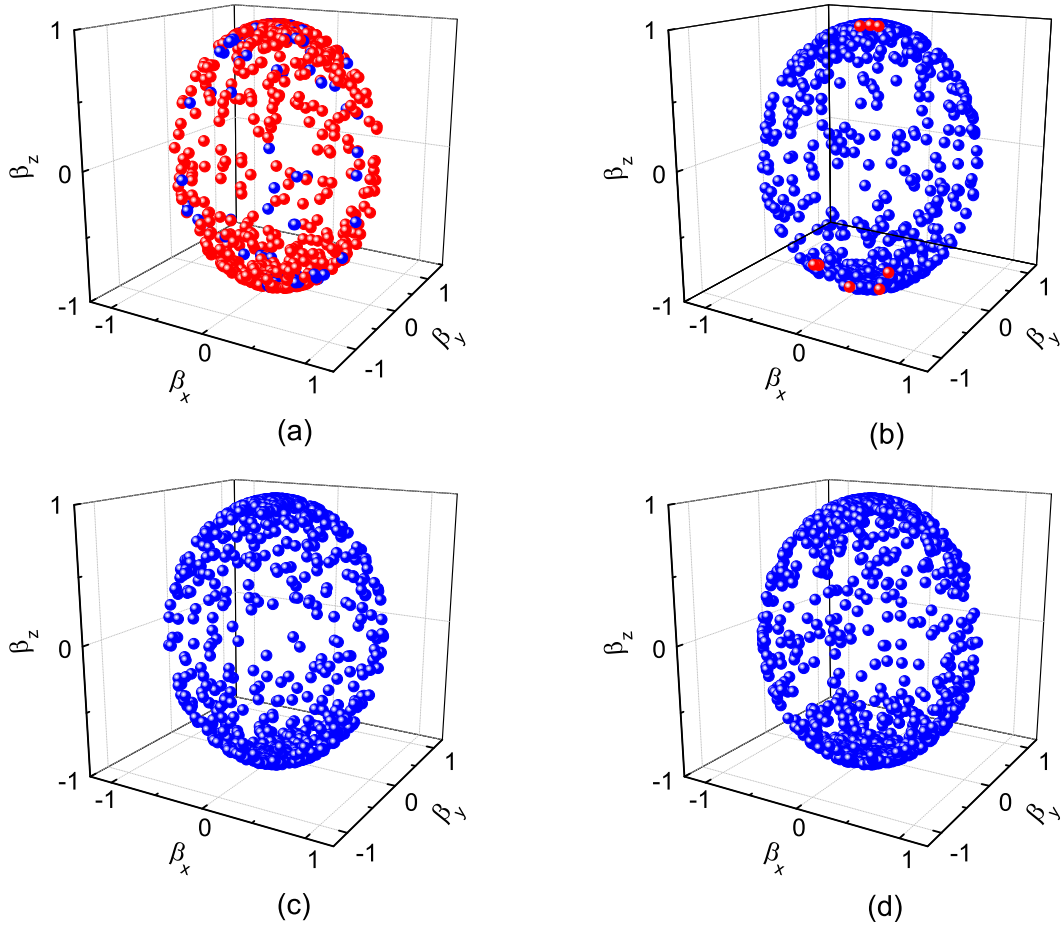
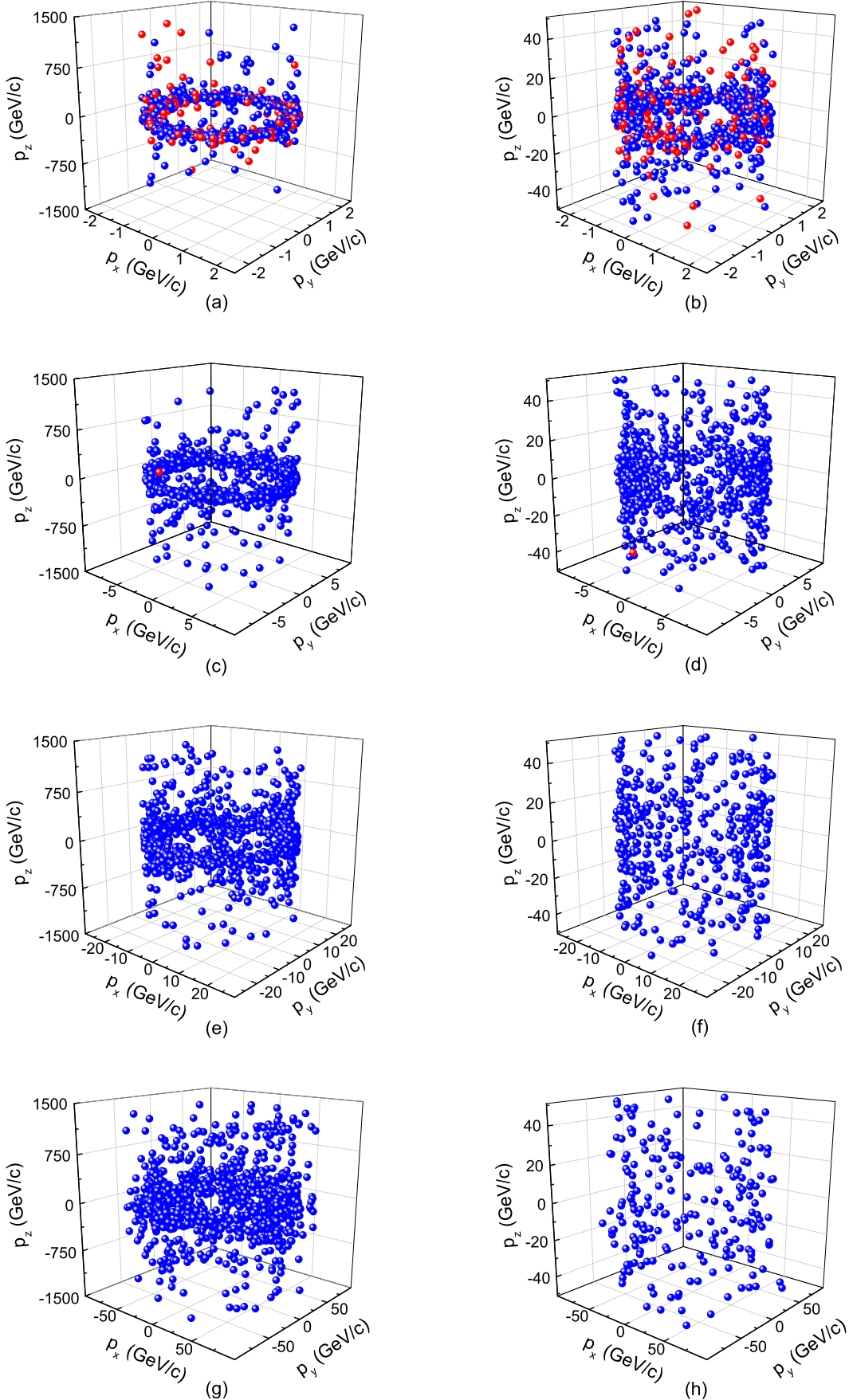


Fig. 6. Same as Figure 5, but showing the results in 0–5% Pb-Pb collisions.



15
 Fig. 7. Event patterns (particle scatter plots) in three-dimensional momentum ($p_x - p_y - p_z$) space at kinetic freeze-out in pp collisions for four transverse momentum intervals: (a)(b) $1.7 < p_T < 2.0$ GeV/c, (c)(d) $6.7 < p_T < 7.7$ GeV/c, (e)(f) $19.9 < p_T < 22.8$ GeV/c, and (g)(h) $59.8 < p_T < 94.8$ GeV/c. The left and right panels display the results in a wide and narrow p_z ranges respectively. The blue and red globules represent the contributions of inverse power-law and Erlang distribution respectively. The number of particles for each panel in the left is 1000.

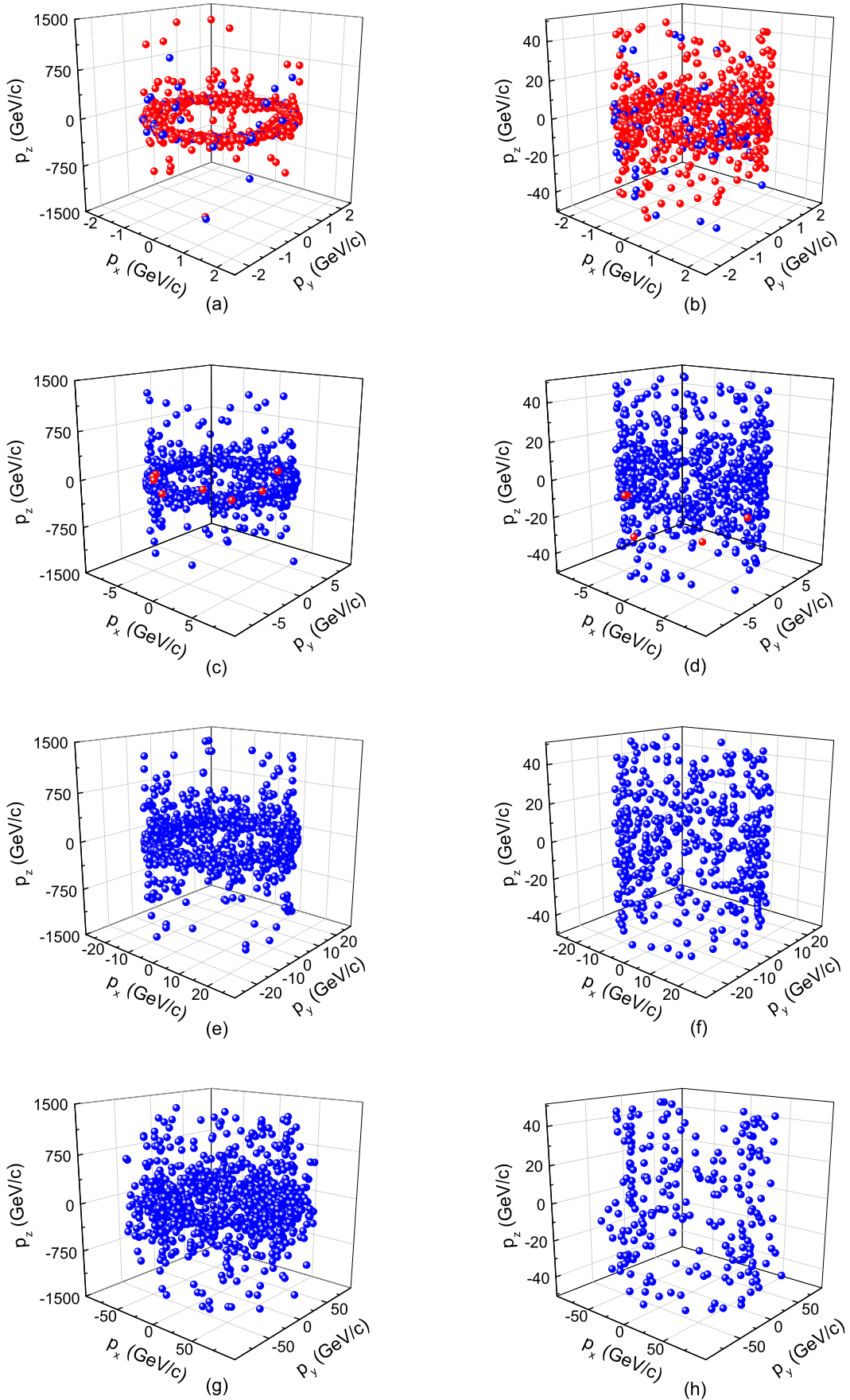


Fig. 8. Same as Figure 7, but showing the results in 0-5% Pb-Pb collisions.

Table 4. Relative yields of particle numbers appearing in different p_T intervals in different types of collisions, where the corresponding scatter plots in pp and 0–5% Pb-Pb collisions are presented in Figures 5 and 6, as well as 7 and 8, respectively. The relative yields in the highest p_T interval are taken to be 1. All the p_T intervals are in the units of GeV/ c .

Type	$1.7 < p_T < 2.0$	$6.7 < p_T < 7.7$	$19.9 < p_T < 22.8$	$59.8 < p_T < 94.8$
pp	2.75×10^6	1.29×10^4	99.6	1
PbPb, 60–80%	2.04×10^6	8.61×10^3	79.6	1
PbPb, 50–60%	1.55×10^6	6.61×10^3	69.5	1
PbPb, 30–40%	1.91×10^6	5.08×10^3	59.4	1
PbPb, 10–20%	2.15×10^6	4.15×10^3	53.0	1
PbPb, 0–5%	2.25×10^6	3.42×10^3	47.5	1

Table 5. Values of the root-mean-squares $\sqrt{p_x^2}$ for p_x , $\sqrt{p_y^2}$ for p_y , and $\sqrt{p_z^2}$ for p_z , as well as the maximum $|p_x|$, $|p_y|$, and $|p_z|$ ($|p_x|_{\max}$, $|p_y|_{\max}$, and $|p_z|_{\max}$) corresponding to the scatter plots in different types of collisions, where the corresponding scatter plots in pp and 0–5% Pb-Pb collisions are presented in Figures 7 and 8 respectively. All the root-mean-squares, maximum momentum components, and p_T intervals are in the units of GeV/ c .

Type	$\sqrt{p_x^2}$	$\sqrt{p_y^2}$	$\sqrt{p_z^2}$	$ p_x _{\max}$	$ p_y _{\max}$	$ p_z _{\max}$
pp						
$1.7 < p_T < 2.0$	1.284 ± 0.015	1.322 ± 0.014	178.6 ± 13.8	1.991	1.996	1.314×10^3
$6.7 < p_T < 7.7$	5.116 ± 0.055	4.970 ± 0.057	253.8 ± 13.9	7.679	7.685	1.369×10^3
$19.9 < p_T < 22.8$	15.187 ± 0.168	14.780 ± 0.173	352.8 ± 14.2	22.730	22.702	1.376×10^3
$59.8 < p_T < 94.8$	50.306 ± 0.620	49.707 ± 0.612	443.5 ± 13.5	93.992	93.443	1.361×10^3
PbPb, 60–80%						
$1.7 < p_T < 2.0$	1.298 ± 0.015	1.304 ± 0.015	191.6 ± 13.6	1.998	1.993	1.354×10^3
$6.7 < p_T < 7.7$	5.135 ± 0.056	4.946 ± 0.058	272.4 ± 14.4	7.655	7.685	1.367×10^3
$19.9 < p_T < 22.8$	15.314 ± 0.164	14.654 ± 0.171	369.8 ± 13.6	22.730	22.787	1.343×10^3
$59.8 < p_T < 94.8$	50.612 ± 0.621	50.001 ± 0.611	467.6 ± 14.3	94.461	94.291	1.371×10^3
PbPb, 50–60%						
$1.7 < p_T < 2.0$	1.302 ± 0.015	1.298 ± 0.015	196.9 ± 14.9	1.995	1.982	1.374×10^3
$6.7 < p_T < 7.7$	5.135 ± 0.056	4.956 ± 0.058	275.0 ± 14.3	7.655	7.685	1.368×10^3
$19.9 < p_T < 22.8$	15.204 ± 0.165	14.766 ± 0.170	372.1 ± 13.7	22.730	22.787	1.361×10^3
$59.8 < p_T < 94.8$	50.042 ± 0.615	50.514 ± 0.614	483.4 ± 14.1	94.461	94.291	1.373×10^3
PbPb, 30–40%						
$1.7 < p_T < 2.0$	1.268 ± 0.015	1.335 ± 0.014	179.3 ± 14.1	1.995	1.996	1.346×10^3
$6.7 < p_T < 7.7$	5.121 ± 0.055	4.968 ± 0.057	242.0 ± 13.7	7.655	7.685	1.360×10^3
$19.9 < p_T < 22.8$	15.292 ± 0.167	14.715 ± 0.174	347.4 ± 14.1	22.730	22.702	1.375×10^3
$59.8 < p_T < 94.8$	50.768 ± 0.621	49.803 ± 0.612	436.0 ± 13.2	94.062	93.583	1.369×10^3
PbPb, 10–20%						
$1.7 < p_T < 2.0$	1.268 ± 0.015	1.335 ± 0.014	179.3 ± 14.1	1.995	1.996	1.346×10^3
$6.7 < p_T < 7.7$	5.121 ± 0.055	4.968 ± 0.057	242.0 ± 13.7	7.655	7.685	1.360×10^3
$19.9 < p_T < 22.8$	15.294 ± 0.167	14.717 ± 0.174	347.5 ± 14.1	22.730	22.702	1.375×10^3
$59.8 < p_T < 94.8$	50.848 ± 0.623	49.886 ± 0.613	436.8 ± 13.3	94.062	93.583	1.369×10^3
PbPb, 0–5%						
$1.7 < p_T < 2.0$	1.288 ± 0.015	1.310 ± 0.014	165.5 ± 14.3	1.995	1.995	1.333×10^3
$6.7 < p_T < 7.7$	5.135 ± 0.055	4.955 ± 0.057	218.6 ± 12.9	7.655	7.685	1.372×10^3
$19.9 < p_T < 22.8$	15.382 ± 0.165	14.633 ± 0.173	343.9 ± 14.5	22.581	22.702	1.376×10^3
$59.8 < p_T < 94.8$	51.362 ± 0.617	49.605 ± 0.620	434.5 ± 13.2	94.097	93.653	1.368×10^3

Table 6. Percentages of particle numbers in the interval $-50 < p_z < 50$ GeV/ c over whole p_z range corresponding to the scatter plots in different p_T intervals in different types of collisions, where the corresponding scatter plots in pp and 0–5% Pb-Pb collisions are presented in Figures 7 and 8 respectively, and “PL” denotes the “power-law”. All the p_T intervals are in the units of GeV/ c .

Type	$1.7 < p_T < 2.0$		$6.7 < p_T < 7.7$		$19.9 < p_T < 22.8$		$59.8 < p_T < 94.8$	
	Inverse PL	Erlang	Inverse PL	Erlang	Inverse PL	Erlang	Inverse PL	Erlang
pp	78%	78%	61%	62%	43%	–	21%	–
PbPb, 60–80%	75%	75%	58%	56%	41%	–	20%	–
PbPb, 50–60%	75%	75%	58%	57%	41%	–	20%	–
PbPb, 30–40%	80%	79%	62%	62%	43%	–	20%	–
PbPb, 10–20%	80%	79%	62%	62%	43%	–	21%	–
PbPb, 0–5%	81%	81%	63%	62%	44%	–	22%	–

By using the same method as that for Figure 7, we can obtain the similar results in Pb-Pb collisions with centrality intervals 60–80%, 50–60%, 30–40%, 10–20%, and 0–5%, respectively. The values of root-mean squares of momentum components and the maximum momentum components are listed in Table 5, and the relative yields of particle numbers appearing in different p_T intervals are listed in Table 4. As another example, to reduce also the size of the paper file, only the scatter plots in the three-dimensional momentum space in 0–5% Pb-Pb collisions are given in Figure 8. Some conclusions obtained from Figure 7 can be obtained from Figure 8 and Tables 4 and 5. In addition, we see intuitively the density change of particle numbers in the three-dimensional momentum space in different p_T intervals at the kinetic freeze-out of the interacting system formed in Pb-Pb collisions with different centrality intervals.

From Figures 5–8 and Tables 2, 3, and 5, one can see that the hard scattering process that is described by the inverse power-law corresponds to a wide $|p_i|$ ($i = x, y$, and z) range, large $\sqrt{p_i^2}$, wide E range, wide $|\beta_{x,y}|$ range, and large $\sqrt{\beta_{x,y}^2}$ due to large momentum transfer and violent collisions between valence quarks. At the same time, because β_z is determined by p_z/E , we are not sure to obtain a wide $|\beta_z|$ range and large $\sqrt{\beta_z^2}$ in the hard scattering process. Instead, a narrow $|\beta_z|$ range and small $\sqrt{\beta_z^2}$ can be generally obtained, which results in a narrow $|y|$ range and small σ_y . The situation of the soft excitation process that is described by the Erlang distribution is opposite. That is, in the soft process, we can obtain a narrow $|p_i|$ range, small $\sqrt{p_i^2}$, narrow E range, narrow $|\beta_{x,y}|$ range, and small $\sqrt{\beta_{x,y}^2}$ due to small momentum transfer and non-violent collisions between gluons and/or sea quarks. Similarly, a wide $|\beta_z|$ range, wide $|y|$ range, and large σ_y can be obtained, too. These differences between the two processes can be partly reflected in the scatter plots.

As an example for comparison, in the three-dimensional velocity space, the event patterns (particle scatter plots) presented in the present work are obviously different from our recent work [41] due to different types of particles being studied. Charged particle scatter plots show that the root-mean-square velocities form an ellipsoid surface with the major axis along the beam direction, and the maximum velocities form a spherical surface. Both the Z boson and quarkonium state scatter plots show that the root-mean square velocities form a rough cylinder surface along the beam direction and the maximum velocities form a fat cylinder surface which has the length being 1.2–2.2 times of diameter, due to their productions being at the initial stage of collisions. Contrastively, charged particles which are mainly pions produce mostly at the intermediate stage of collisions and suffer particularly the processes of thermalization and expansion of the interacting system. Generally, different scatter plots reflect different production stages of different types of particles. The present work shows similar result to our another recent work [40] which studies the scatter plots of net-baryons which are a part of charged particles and suffer the thermalization and expansion of the system.

We would like to point out that a correct description of the low p_T part using the Erlang distribution should seemingly include the effect of transverse flow. In fact, the parameters extracted from the p_T spectra contain naturally the contribution of flow effect, though the flow effect and thermal motion are tangled each other. Only in the case of extracting the kinetic freeze-out temperature, the flow effect should be eliminated [44–46]. The present

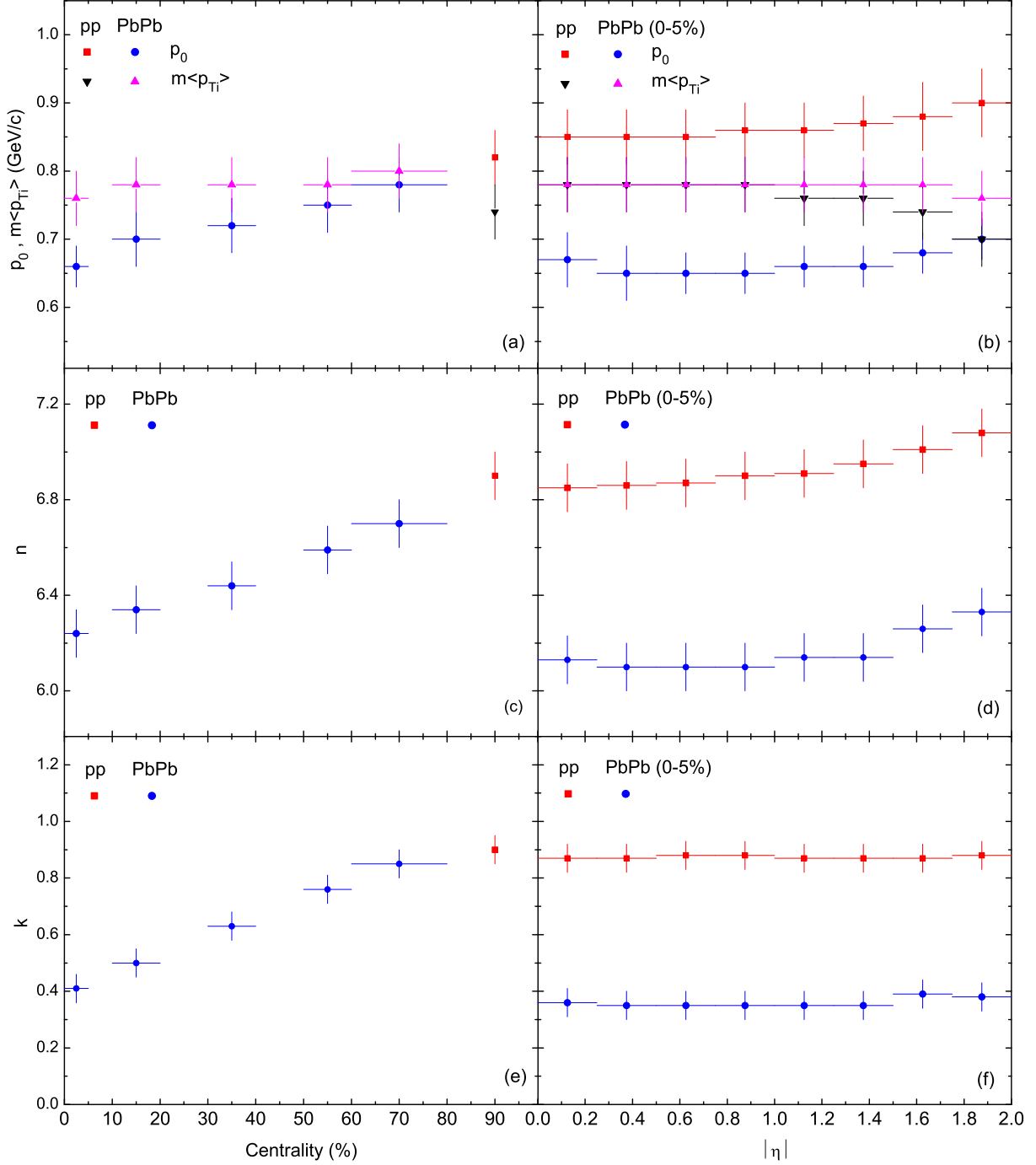


Fig. 9. Left: Dependences of (a) p_0 and $m\langle p_{Ti} \rangle$, (c) n , and (e) k on centrality in pp and Pb-Pb collisions at 2.76 TeV, where the results corresponding to pp collisions are listed in 90% centrality for comparisons. Right: Dependences of (b) p_0 and $m\langle p_{Ti} \rangle$, (d) n , and (f) k on $|\eta|$ in pp and 0–5% Pb-Pb collisions. Different symbols represent different collisions and quantities shown in the panels, where the idiographic values are taken from Table 1.

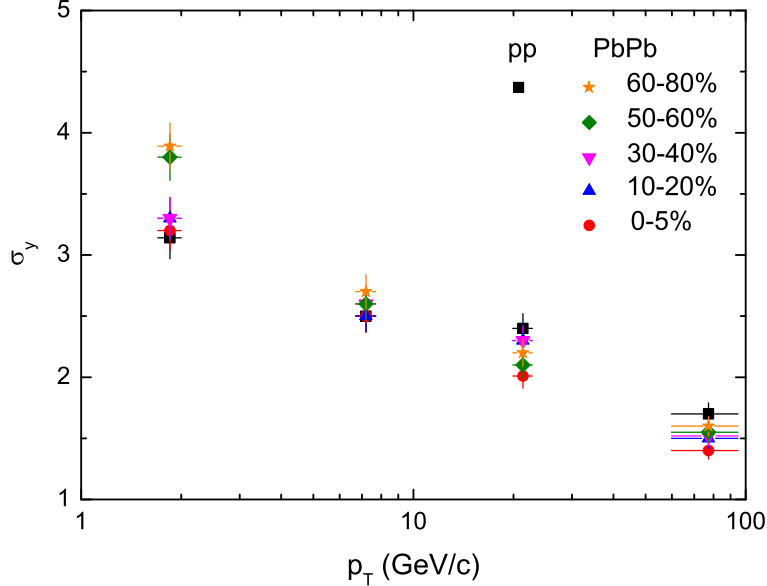


Fig. 10. Dependence of σ_y on p_T in pp and Pb-Pb collisions at 2.76 TeV. Different symbols represent different collisions shown in the panel, where the idiographic values are taken from Table 2.

work focuses mainly on quantities at the kinetic freeze-out, but it does not include the kinetic freeze-out temperature which needs more spectra of identified particles. Both the contributions of flow effect and thermal motion are contained in the extraction of parameters, though the two contributions are not distinguished. To severally understand the contributions of flow effect and other non-flow effects such as thermal motion, more than one disentangling methods are used in literature [47, 48]. In our very recent works [44–46], an alternative method is used to disentangle the two effects.

In the alternative method, the collective expansion of source and random thermal motion of particles are naturally disentangled to be the mean transverse flow velocity and kinetic freeze-out temperature, respectively. The mean transverse flow velocity can be extracted from the slope of the mean transverse momentum ($\langle p_T \rangle$) curve as a function of mean moving mass (\overline{m}) when plotting $\langle p_T \rangle$ versus \overline{m} , and the kinetic freeze-out temperature can be extracted from the intercept of the effective temperature (T) curve as a function of m_0 when plotting T versus m_0 [46], where T is usually regarded as the inverse slopes of p_T spectra and m is also used to denote the moving mass. To use this alternative method, we need at least p_T spectra of pions, kaons, and protons in the same experimental condition. As statistical results, the flow effect and thermal motion can be disentangled in principle. In the case of disentangling the two effects, their several contributions can be obtained. It is regretful that the charged particle spectra discussed in the present work are not suitable to use the alternative method.

To study in detail the tendencies of free parameters, the left panel in Figure 9 shows the dependences of (a) p_0 and $m\langle p_{Ti} \rangle$, (c) n , and (e) k on centrality in pp and Pb-Pb collisions at 2.76 TeV, where the results corresponding to pp collisions are listed in 90% centrality for comparisons. The right panel in Figure 9 shows the dependences of (b) p_0

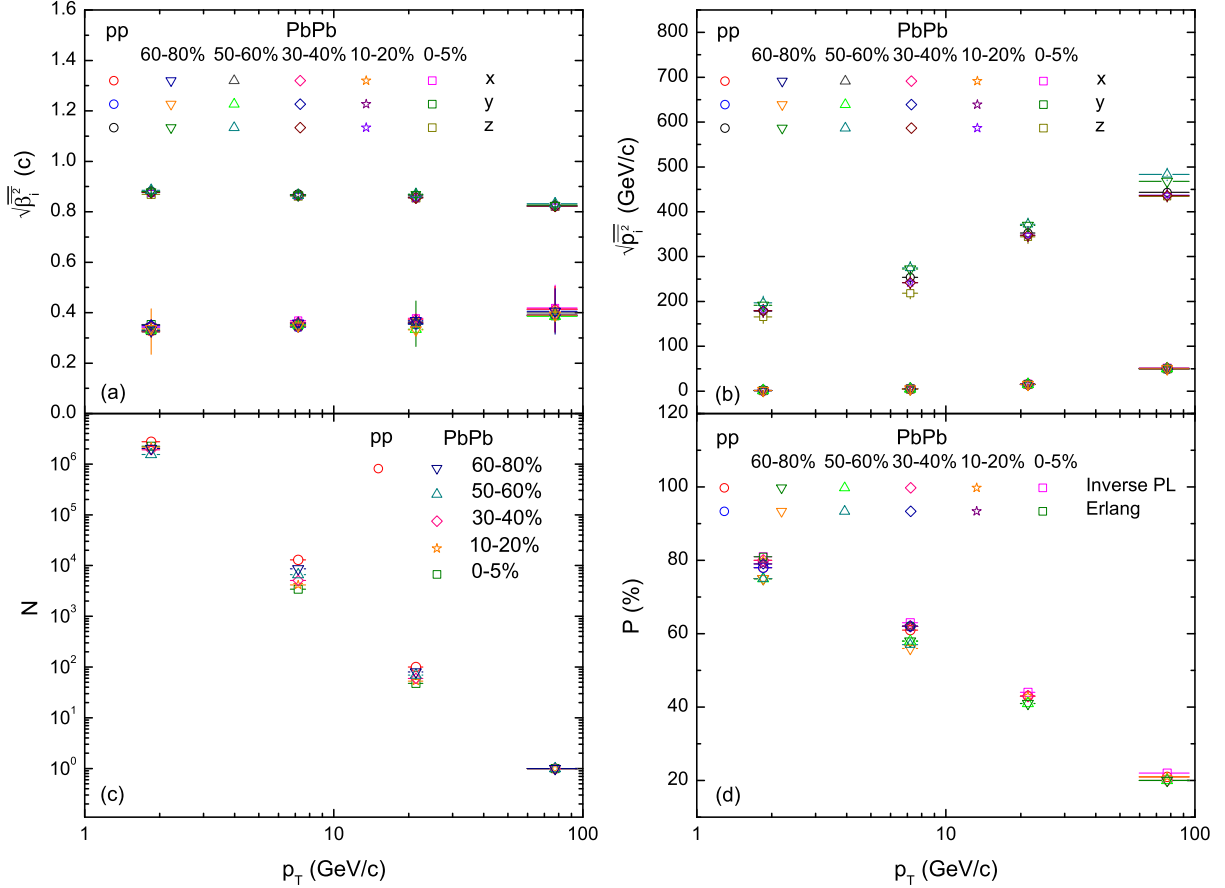


Fig. 11. Dependences of (a) $\sqrt{\beta_i^2}$ ($i = x, y,$ and z), (b) $\sqrt{p_i^2}$, (c) relative particle number N , and (d) percentage P in $-50 < p_z < 50$ GeV/ c over whole p_z range on p_T in pp and Pb-Pb collisions at 2.76 TeV. Different symbols represent different collisions and quantities shown in the panels, where the idiographic values are taken from Tables 3, 5, 4, and 6, respectively.

and $m\langle p_{T_i} \rangle$, (d) n , and (f) k on $|\eta|$ in pp and 0–5% Pb-Pb collisions. Figure 10 shows the dependence of σ_y on p_T in pp and Pb-Pb collisions. In Figures 9 and 10, different symbols represent different collisions and quantities shown in the panels, where the idiographic values are taken from Tables 1 and 2. One can see that p_0 , n , and k increase with the decrease of centrality. $m\langle p_{T_i} \rangle$ does not show an obvious tendency with the centrality. In pp collisions, p_0 increases slightly and $m\langle p_{T_i} \rangle$ decreases slightly with the increase of $|\eta|$. In 0–5% Pb-Pb collisions, p_0 and $m\langle p_{T_i} \rangle$ do not show an obvious tendency with the increase of $|\eta|$. In both pp and 0–5% Pb-Pb collisions, n increases slightly and k does not change with the increase of $|\eta|$. The tendency that σ_y decreases with the increases of p_T does not obviously depend on system size and collision centrality.

We can explain the characteristics of some parameters. For hard process, the values of p_0 , n , and k in pp or peripheral Pb-Pb collisions are greater than those in central Pb-Pb collisions due to more successive nucleon-nucleon collisions in the latter one. Although the successive nucleon-nucleon collisions can produce more particles, the violent degree in head-on scattering between valence quarks is reduced, which renders small values of parameters. For soft process, the values of $m\langle p_{T_i} \rangle$ in collisions for different sizes and centralities are close to each other due to the similar excitation degree between gluons and/or sea quarks and the similar flow effect. On the dependences of p_0 and $m\langle p_{T_i} \rangle$ on $|\eta|$ in pp collisions, different tendencies appear due to different participant partons. In 0–5% Pb-Pb collisions, the different tendencies are reduced due to more intranuclear cascade collisions. As for n and k , the same tendency appears for both pp and 0–5% Pb-Pb collisions, though the values for pp collisions are greater than those for 0–5% Pb-Pb collisions due to absent intranuclear process in pp collisions. The decrescent tendency of σ_y with increasing p_T is a natural result, where small p_T corresponds to small/large angle and large $|\eta|$, and large p_T corresponds to middle angle and small $|\eta|$. For the production of charged particles, the dependence of free parameters on collision centrality is a reflection of cold nuclear effect which results from different numbers of multi-scattering in cold nuclei or spectators with different sizes. The larger the spectator is, the more the parameters depend.

According to Tables 3–6, we obtain the dependences of $\sqrt{\beta_i^2}$, $\sqrt{p_i^2}$, relative particle number N , and percentage P in $-50 < p_z < 50$ GeV/ c over whole p_z range, on p_T in Figure 11, where different symbols represent different collisions and quantities shown in the panels. One can see that $\sqrt{\beta_x^2}$ and $\sqrt{\beta_y^2}$ increase slightly with the increase of p_T , and they are almost the same for different sizes and centralities of collisions. $\sqrt{\beta_z^2}$ decreases slightly with the increase of p_T , and it is almost the same for different sizes and centralities. The situations for $\sqrt{p_x^2}$ and $\sqrt{p_y^2}$ are the same as those for $\sqrt{\beta_x^2}$ and $\sqrt{\beta_y^2}$. $\sqrt{p_z^2}$ increases obviously with the increase of p_T , where the values for different sizes and centralities are distinguishable, though the characteristic of distinction is not obvious. N decreases quickly with the increase of p_T , and in some cases the values are almost the same for different sizes and centralities. P also decreases with the increase of p_T for both inverse power-law and Erlang distribution, and in some cases the values are very close to each other for different sizes, centralities, and functions. The characteristics presented in Figure 11 are determined by the parameters presented in Tables 1 and 2 (or Figures 9 and 10).

From the above discussions, although one can see a very complete analysis of p_T and y spectra of charged particles produced in pp and Pb-Pb collisions at the LHC, it seems that the model used for this analysis does not have a strong theoretical basis. In fact, we have used a hybrid model in which each part has its reason. For the p_T spectra, it considers the superposition of a polynomial inverse power-law which is suggested by the QCD calculus [18–20] and an exponential-like Erlang distribution which is resulted from the multisource thermal model [17]. For the y spectra, it considers a Gaussian function which is resulted from the Landau hydrodynamic model [21–24]. Both the functions for p_T and y spectra look very simple, useful, and efficient. In particular, the two-component function for p_T spectra contains both the contributions of hard scattering and soft excitation processes which correspond to violent collisions between valence quarks and non-violent collisions between gluons and/or sea quarks respectively. At the same time, the hard and soft processes result from large and small momentum transfers, and contribute in wide and narrow p_T regions, respectively. At the considered energy, in most cases, the hard process has a large contribution, which is different from that at low energy.

4 Conclusions

We summarize here our main observations and conclusions.

(a) The transverse momentum and pseudorapidity spectra of charged particles produced in pp collisions at $\sqrt{s} = 2.76$ TeV and in Pb-Pb collisions with different centrality intervals at $\sqrt{s_{NN}} = 2.76$ TeV at the LHC are described by the hybrid model, in which the two-component p_T distribution (which contains the inverse power-law and the Erlang distribution) and the Gaussian y distribution are used. The inverse power-law is based on the QCD calculus, the Erlang distribution is resulted from the multisource thermal model, and the Gaussian y distribution is resulted from the Landau hydrodynamic model. The modelling results are in agreement with the experimental data of the ATLAS Collaboration.

(b) In the hybrid model, both the functions for p_T and y spectra look very simple, useful, and efficient. In particular, the two-component function for p_T spectra contains both the contributions of hard scattering and soft excitation processes which correspond to violent collisions between valence quarks and non-violent collisions between gluons and/or sea quarks respectively. Not only for the hard scattering process but also for the soft excitation process, the numbers of participant partons are two, in which one is the projectile parton and the other one is the target parton. The hard scattering process contributes a wide p_T range, and the soft excitation process contributes a narrow p_T range. In the considered collisions at the LHC, the hard process has a large contribution in most cases.

(c) The parameters p_0 , n , and k increase with the decrease of centrality. $m\langle p_{Ti} \rangle$ does not show an obvious tendency with the centrality. For hard process, the values of p_0 , n , and k in pp or peripheral Pb-Pb collisions are greater than those in central Pb-Pb collisions due to more successive nucleon-nucleon collisions in the latter one. For soft process, the values of $m\langle p_{Ti} \rangle$ in collisions for different sizes and centralities are close to each other due to the similar excitation degree between gluons and/or sea quarks and the similar flow

effect. The tendency that σ_y decreases with the increase of p_T is a natural result due to small p_T corresponding to small/large angle and large $|\eta|$, and large p_T corresponding to middle angle and small $|\eta|$.

(d) In pp collisions, p_0 slightly increases and $m\langle p_{Ti} \rangle$ slightly decreases with the increase of $|\eta|$. In 0–5% Pb-Pb collisions, p_0 and $m\langle p_{Ti} \rangle$ do not show an obvious tendency with the increase of $|\eta|$. On the dependence of p_0 and $m\langle p_{Ti} \rangle$ on $|\eta|$ in pp collisions, different tendencies appear due to different participant partons (valence quarks versus gluons and/or sea quarks). In 0–5% Pb-Pb collisions, the different tendencies in the dependence of p_0 and $m\langle p_{Ti} \rangle$ on $|\eta|$ are reduced due to more intranuclear collisions. In both pp and 0–5% Pb-Pb collisions, n slightly increases and k does not change with the increase of $|\eta|$. The values of n and k for pp collisions are greater than those for 0–5% Pb-Pb collisions due to absent intranuclear process in pp collisions.

(e) Based on the parameter values extracted from p_T and η spectra, the event patterns (particle scatter plots) in the three-dimensional velocity and momentum spaces are obtained. In particular, $\sqrt{\beta_x^2} \approx \sqrt{\beta_y^2} \ll \sqrt{\beta_z^2}$, $|\beta_x|_{\max} \approx |\beta_y|_{\max} \approx |\beta_z|_{\max} \approx 1$, $\sqrt{p_x^2} \approx \sqrt{p_y^2} \ll \sqrt{p_z^2}$, and $|p_x|_{\max} \approx |p_y|_{\max} \ll |p_z|_{\max}$. The root-mean-square velocities form an ellipsoid surface with the major axis along the beam direction, and the maximum velocities form a spherical surface. Viewing the wide p_z range, most particles constitute a circle-like region surrounded by a few particles; and viewing the narrow p_z range, particles constitute a cylinder surface surrounded by a few particles. The severally relative sizes of $\sqrt{\beta_i^2}$, $|\beta_i|_{\max}$, $\sqrt{p_i^2}$, and $|p_i|_{\max}$ for different i , as well as the related characteristics are determined by the extracted parameters and isotropic assumption in transverse plane.

(f) Further, based on the parameters extracted above, $\sqrt{\beta_x^2}$ and $\sqrt{\beta_y^2}$ slightly increase with the increase of p_T , and they are almost the same for different sizes and centralities of collisions. The situations for $\sqrt{p_x^2}$ and $\sqrt{p_y^2}$ are the same as those for $\sqrt{\beta_x^2}$ and $\sqrt{\beta_y^2}$. $\sqrt{\beta_z^2}$ slightly decreases with the increase of p_T , and it is almost the same for different sizes and centralities. $\sqrt{p_z^2}$ obviously increases with the increase of p_T , where the values for different sizes and centralities are distinguishable, though the characteristic of distinction is not obvious. Naturally, the characteristics of $\sqrt{\beta_i^2}$ and $\sqrt{p_i^2}$ are determined by the extracted parameters, which are determined by many factors such as the number of intranuclear cascade collisions, type of participant partons, dependence of collision centrality (number of multi-scattering in cold nucleus or spectator), and others.

(g) The hard scattering process corresponds to a wide $|p_i|$ range, large $\sqrt{p_i^2}$, wide E range, wide $|\beta_{x,y}|$ range, large $\sqrt{\beta_{x,y}^2}$, narrow $|\beta_z|$ range, small $\sqrt{\beta_z^2}$, narrow $|y|$ range, and small σ_y . The situation of the soft excitation process is opposite. These differences between the two processes can be partly reflected in the scatter plots in three-dimensional velocity and momentum spaces where the hard process corresponds to wider range. The reason that causes these differences is different interacting mechanisms. Generally, the hard scattering process is produced due to violent collisions between valence quarks where large momentum transfer occurs. The soft excitation process is produced due to non-violent collisions between gluons and/or sea quarks where small momentum transfer occurs.

(h) Different types of particles correspond to different scatter plots due to different pro-

duction stages. The scatter plots of charged particles are different from those of Z bosons and quarkonium states discussed in our recent work [41] in which the root-mean square velocities show a rough cylinder surface and the maximum velocities form a fat cylinder surface in the three-dimensional velocity space, due to the productions of Z bosons and quarkonium states being at the initial stage of collisions, while charged particles which are mainly pions produce mostly at the intermediate stage of collisions and suffer particularly the processes of thermalization and expansion of the interacting system. Combining with our recent works [40, 41], we have provided a reference in methodology which displays event patterns (particle scatter plots) for different particles in three-dimensional velocity and momentum spaces or other available spaces based on the transverse momentum and pseudorapidity or rapidity spectra of considered particles.

Acknowledgments

This work was supported by the National Natural Science Foundation of China under Grant No. 11575103.

References

- [1] Song H, Bass S A, Heinz U, Hirano T and Shen C 2011 *Phys. Rev. Lett.* **106** 192301
- [2] Andronic A 2014 *Int. J. Mod. Phys. A* **29** 1430047
- [3] Novak J, Novak K, Pratt S, Vredevoogd J, Coleman-Smith C and Wolpert R 2014 *Phys. Rev. C* **89** 034917
- [4] Qin G-Y, 2015 *Int. J. Mod. Phys. E* **24** 1530001
- [5] Ding H-T, Karsch F and Mukherjee S 2015 *Int. J. Mod. Phys. E* **24** 1530007
- [6] Lacey R A 2015 *Phys. Rev. Lett.* **114** 142301
- [7] Chatterjee S, Das S, Kumar L, Mishra D, Mohanty B, Sahoo R and Sharma N 2015 *Adv. High Energy Phys.* **2015**, 349013
- [8] Ning P-Z, Li L, Min D-F 2003 *Foundation of Nuclear Physics: Nucleons and Nuclei*, Higher Education Press, Beijing, China
- [9] Dermer C D 1984 *Astrophys. J.* **280** 328
- [10] Tsallis C 1988 *J. Stat. Phys.* **52** 479
- [11] Biró T S, Purcsel G and Ürmössy K 2009 *Eur. Phys. J. A* **40** 325
- [12] Cleymans J and Worku D 2012 *Eur. Phys. J. A* **48** 160
- [13] Schwinger J 1951 *Phys. Rev.* **82** 664
- [14] Wang R C and Wong C Y 1988 *Phys. Rev. D* **38** 348
- [15] Braun-Munzinger P, Redlich K and Stachel J 2004 in *Quark-Gluon Plasma 3*, edited by Hwa R C and Wang X-N, World Scientific, Singapore, arXiv:nucl-th/0304013
- [16] Wong C-Y 1994 *Introduction to High Energy Heavy Ion Collisions*, World Scientific, Singapore
- [17] Liu F-H, Gao Y-Q, Tian T and Li B-C 2014 *Eur. Phys. J. A* **50** 94
- [18] Odorico R 1982 *Phys. Lett. B* **118** 151
- [19] Arnison G *et al.* (UA1 Collaboration) 1982 *Phys. Lett. B* **118** 167

- [20] Biyajima M, Mizoguchi T and Suzuki N 2016 arXiv:1604.01264 [hep-ph]
- [21] Landau L D 1953 *Izvestiya Akademii Nauk: Series Fizicheskikh* **17** 51 in *English-Translation: Collected Papers of L. D. Landau*, Edited by Ter-Haarp D 1965, p. 569, Pergamon, Oxford, UK
- [22] Belenkij S Z and Landau L D 1955 *Soviet Physics Uspekhi* **56** 309 in *English-Translation: Collected Papers of L. D. Landau*, Edited by Ter-Haarp D 1965, p. 665, Pergamon, Oxford, UK
- [23] Steinberg P A 2005 *Nucl. Phys. A* **752** 423
- [24] Jiang Z-J, Deng H-P, Zhang Y and Zhang H-L 2015 *Nucl. Phys. Rev. (China)* **32** 398
- [25] Abgrall N *et al.* (NA61/SHINE Collaboration) 2014 *Eur. Phys. J. C* **74** 2794
- [26] Gao L-N, Liu F-H, Sun Y, Sun Z and Lacey R A 2016 arXiv:1607.00611 [hep-ph]
- [27] D'innocenzo A, Ingrosso G and Rotelli P 1980 *Lettere al Nuovo Cimento* **27** 457
- [28] D'innocenzo A, Ingrosso G and Rotelli P 1979 *Lettere al Nuovo Cimento* **25** 393
- [29] D'innocenzo A, Ingrosso G and Rotelli P 1980 *Il Nuovo Cimento A* **55** 417
- [30] D'innocenzo A, Ingrosso G and Rotelli P 1978 *Il Nuovo Cimento A* **44** 375
- [31] Chou K-C, Liu L-S and Meng T-C 1983 *Phys. Rev. D* **28** 1080
- [32] Liu L-S and Meng T-C 1983 *Phys. Rev. D* **27**, 2640
- [33] Wolschin G 1999 *Eur. Phys. J. A* **5** 85
- [34] Wolschin G 2011 *EPL* **95** 61001
- [35] Wolschin G 2013 *J. Phys. G* **40** 045104
- [36] Wolschin G 2007 *Prog. Part. Nucl. Phys.* **59** 374
- [37] Cleymans J 2008 *J. Phys. G* **35** 044017
- [38] Becattini F and Cleymans J 2007 *J. Phys. G* **34** S959
- [39] Marques L, Cleymans J and Deppman A 2015 *Phys. Rev. D* **91** 054025
- [40] Chen Y-H, Zhang G-X and Liu F-H 2015 *Adv. High Energy Phys.* **2015** 614090
- [41] Chen Y-H, Liu F-H and Lacey R A 2016 *Adv. High Energy Phys.* **2016** 9876253
- [42] Aad G *et al.* (The ATLAS Collaboration) 2015 *JHEP* **1509** 050
- [43] Miller M L, Reygers K, Sanders S J and Steinberg P 2007 *Ann. Rev. Nucl. Part. Sci.* **57** 205
- [44] Wei H-R, Liu F-H and Lacey R A 2016 *Eur. Phys. J. A* **52** 102
- [45] Lao H-L, Wei H-R, Liu F-H and Lacey R A 2016 *Eur. Phys. J. A* **52** 203
- [46] Wei H-R, Liu F-H and Lacey R A 2016 *J. Phys. G* **43** 125102
- [47] Schnedermann E, Sollfrank J and Heinz U 1993 *Phys. Rev. C* **48** 2462
- [48] Adler *et al.* (PHENIX Collaboration) 2004 *Phys. Rev. C* **69** 034909